Phase relationship in laminar channel flow controlled by traveling-wave-like blowing or suction

Hiroya Mamori,[1] Koji Fukagata,[1] and Jerôme Hoepffner[2]

[1]*Department of Mechanical Engineering, Keio University, Yokohama 223-8522, Japan*
[2]*Institut D'Alembert, UPMC, 75252 Paris Cedex 05, France*

The phase relationship between the streamwise and the wall-normal velocity disturbances induced by a traveling-wave-like blowing or suction control [T. Min *et al.*, J. Fluid Mech. **558**, 309 (2006)] in a two-dimensional laminar Poiseuille flow is investigated. The investigation is done by solving the linearized Navier-Stokes equation and by using the identity equation between the skin-friction drag and the Reynolds shear stress [K. Fukagata *et al.*, Phys. Fluids **14**, L73 (2002)]. It has been known that a traveling wave creates a non-quadrature between the velocity disturbances and generates the positive phase shift of the streamwise velocity disturbance in the case of a skin-friction drag reduction. The present analysis further reveals that this non-quadrature consists of an inviscid base phase relationship and a near-wall phase shift induced by the viscosity. The analogy between the present control and Stokes' second problem is discussed. The thickness of the near-wall region in which the viscous phase shift takes place is found to be scaled similarly to the Stokes' second problem.

I. INTRODUCTION

Reduction in the skin-friction drag in turbulent flow is of great importance for energy utilization: the friction drag contributes to, e.g., about 50%, 90%, and 100 % of the total drag in commercial aircrafts, underwater vehicles, and pipelines, respectively [1]. Since 1990s, different active control methods for the skin-friction drag reduction have been proposed, e.g., wall oscillations [2], blowing or suction from the walls [3], and deformation of the walls [4,5].

Because the quasistreamwise vortex in the region near the wall exchanges the momentum, the skin-friction drag and the Reynolds shear stress (RSS) significantly increase in wall-bounded turbulent flows. In fact, there is an identity equation relating the RSS and the skin friction [6,7]. For a fully developed channel flow, the identity equation for the dimensionless friction drag, D, reads as

$$D = \underbrace{2}_{D_{lam}} + \underbrace{\frac{3}{2}\mathrm{Re}\int_{-1}^{1}(-y)(-\overline{u'v'})dy}_{\Delta D}.$$
(1)

Here, the Reynolds number, $\mathrm{Re} = U_c\delta/\nu$, is defined based on the centerline velocity, U_c, and the channel half width, δ; $-\overline{u'v'}$ is the RSS and y is the wall normal coordinate extending from $y = -1$ (lower wall) to $y = 1$ (upper wall). This equation indicates that the skin-friction drag is divided clearly into the laminar contribution, $D_{lam} = 2$, and the drag increment, ΔD, which is the integration of the y-weighted RSS. More surprisingly, this equation implies that a friction drag below the laminar level (i.e., sublaminar drag) is achieved if $\Delta D < 0$ [6].

Based on this implication, Min *et al.* [8] proposed a predetermined control method by which sublaminar drag can be achieved without using any sensors. Their method assumes the local blowing or suction velocity from the walls, v_w, as

$$v_w = a\cos[k(x - ct)],$$
(2)

where x and t denote the streamwise coordinate and the time, respectively. The parameters a, k, and c represent the ampli-

tude, the wave number, and the wave speed of the traveling wave, respectively. Min *et al.* [8] predicted the amount of drag reduction by coupling the linear analysis and Eq. (1). The sublaminar drag was achieved by upstream traveling wave ($c < 0$) and in such cases negative RSS (if the RSS in ordinary turbulent channel flows is called positive) is created in the regions near the walls. Min *et al.* [8] also confirmed the drag reduction effect in a fully developed turbulent channel flow by means of direct numerical simulation (DNS). The mechanism of the skin-friction drag reduction was also discussed by the two-dimensional simulation of channel flow under zero mean pressure gradient. It was found that the net mass flux in the streamwise direction was induced by the upstream traveling wave, which is as pointed out by Marusic *et al.* [9] equivalent to the skin-friction drag reduction in the channel flow under a constant mass flow rate. This net mass flux was induced by the RSS caused by the positive phase shift of streamwise velocity disturbance. Hoepffner and Fukagata [10] confirmed this pumping effect by simulating flows without imposing a mean pressure gradient. They showed that the traveling-wave-like blowing or suction pumps in the backward direction, while the similar deformation pumps in the forward direction. They also explained the dynamical mechanism of pumping by analyzing the streamlines and trajectories of fluid particles.

The major drawback of the control of Min *et al.* [8] may be the much smaller gain (i.e., more expensive control cost) than that of the existing feedback control schemes [11,12]. Under the constant flow rate condition, the gain of upstream traveling wave control is on the order of 1–10, while that of the existing feedback control schemes is on the order of 100–1000. According to the very recent study by Lieu *et al.* [13] (see also, Moarref and Jovanović [14]), the gain of the upstream traveling wave control can be even smaller under the constant pressure gradient condition instead of constant flow rate. A plausible reason for the small gain is that the upstream traveling wave does not stabilize the flow, as was revealed by Lee *et al.* [15] through the stability analysis. Lee *et al.* [15] also showed that most disturbances become highly
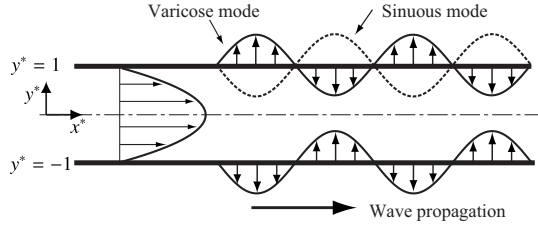
FIG. 1. Flow geometry and schematic of control input.

unstable at the wave speed of $c \approx 0.4$. Min's control, however, is still attractive for realization of active turbulent drag reduction because it does not require massive microsensors [16], which is one of the biggest hurdles for feedback controls to be applied in reality.

The present work is an extension of the studies of Min *et al.* [8] and Hoepffner and Fukagata [10]. In order to obtain a unified explanation on the drag reduction effect by the traveling-wave-like blowing or suction in a laminar channel flow, wide ranges of control parameters (Reynolds number, wave number, and wave speed) are examined and analyzed through a detailed phase analysis. As will be shown later, these effects can be scaled similarly to the Stokes' second problem. In order to demonstrate the validity of this scaling in a different control mode, we also consider the sinuous mode in addition to the varicose mode which has been considered by Min *et al.* [8] and Hoepffner and Fukagata [10].

It is also worth noting that drag reduction control of a laminar channel flow does not make sense from the practical viewpoint. Bewley [17] and Fukagata *et al.* [18] mathematically proved that under a constant flow rate the lower bound of driving power (i.e., sum of pumping and actuation powers) is the pumping power of the laminar channel flow. Namely, the total power can never be saved when control is applied to a laminar channel flow even if a sublaminar drag is achieved. Nevertheless, we study the mechanism of the control of Min *et al.* [8] using a laminar flow as an important step toward the comprehensive understanding of control effects in turbulent flows. The use of laminar flow may be justified by the following reasons: (1) the primary effect of control, i.e., production of the "negative" Reynolds shear stress (or, in other words, pumping from the walls [10]), is considered common to laminar and turbulent flows; and of course, (2) it is simpler than a turbulent flow.

II. LINEAR ANALYSIS

A two-dimensional channel flow is considered. The governing equations are two-dimensional and incompressible continuity and Navier-Stokes equations. Figure 1 shows the flow geometry, the coordinate systems, and the control input. All quantities are made dimensionless by using the centerline velocity, U_c, and the channel half-height, δ. The velocity components in the x^* (streamwise) and y^* (wall-normal) directions are denoted as u and v, respectively. The pressure is denoted as p. The asterisk denotes the fixed coordinates in contrast to the moving coordinates introduced later. The base flow, U, is set to be the laminar Poiseuille profile, i.e., $U = 1 - y^{*2}$.

The periodic boundary condition is employed in the streamwise direction. The no-slip condition is imposed for the streamwise velocity at the wall. As a control input, the wall-normal velocity at the wall is given as a traveling-wave-like blowing or suction. Two wave modes are considered for the traveling wave: the varicose mode and the sinuous mode. The varicose mode corresponds to two solid lines in Fig. 1, which reads [8] as

$$v_{w\pm} = \mp\, a\, \cos[k(x^* - ct^*)],$$ (3)

where v_{w+} and v_{w-} are the wall-normal velocity at the upper and the lower walls, respectively. Namely, the surface wall-normal velocities are in phase with opposite sign. In contrast, the sinuous mode is the combination of the solid line at the lower wall and the dotted line at the upper wall in Fig. 1, which reads as

$$v_{w\pm} = \pm\, a\, \cos[k(x^* - ct^*)].$$ (4)

The surface wall-normal velocities are in phase.

The problem can be reduced into a steady problem by introducing a coordinate transformation from the fixed coordinates to the coordinates traveling with the wave, i.e., $x := x^* - ct^*$, $y := y^*$, $t := t^*$ [19]. The boundary conditions [Eqs. (3) and (4)] in the moving coordinates read

$$v_{w\pm} = \begin{cases} \mp\, a\, \cos(kx) & \text{varicose mode} \\ \pm\, a\, \cos(kx) & \text{sinuous mode.} \end{cases}$$ (5)

The unsteady term of incompressible Navier-Stokes equation is transformed as

$$\frac{\partial}{\partial t^*} = \frac{\partial}{\partial t} - c\frac{\partial}{\partial x}.$$ (6)

Because the flow is steady due to the steady boundary condition, the first term in the right-hand side of Eq. (6) vanishes.

The governing equations are linearized: $u = U + u'$, $v = v'$, and $p = P + p'$ are substituted into the governing equations and the high-order terms of disturbance are neglected. Here, U and P denote the velocity and pressure of the base flow, respectively, and the prime denotes the disturbance component. The linearized disturbance equations read as

$$\frac{\partial u'}{\partial x} + \frac{\partial v'}{\partial y} = 0,$$ (7)

$$-c\frac{\partial u'}{\partial x} + U\frac{\partial u'}{\partial x} + v'\frac{\partial U}{\partial y} = -\frac{\partial p'}{\partial x} + \frac{1}{\text{Re}}\nabla^2 u',$$ (8)

$$-c\frac{\partial v'}{\partial x} + U\frac{\partial v'}{\partial x} = -\frac{\partial p'}{\partial y} + \frac{1}{\text{Re}}\nabla^2 v'.$$ (9)

Equations (7)–(9) are discretized by using the Fourier transformation in the streamwise direction and the Chebyshev collocation method in the wall-normal direction. These equations can be expressed as a system matrix equation; thus, the solution can easily be obtained. Details of the numerical discretization are presented in the Appendix.
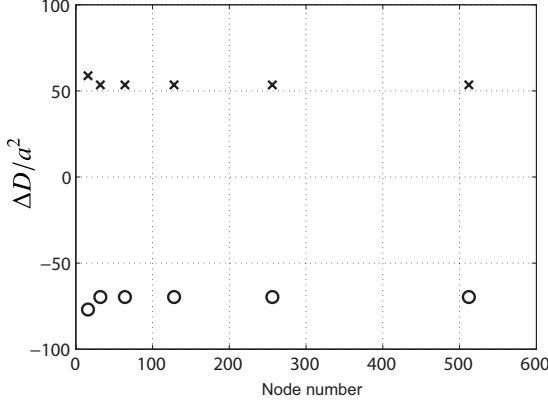
FIG. 2. Node number dependency of $\Delta D/a^2$ for $k=0.5$, $c=-2$, and Re=2000: circle, varicose mode; cross, sinuous mode.

According to the amplitude expansion of flow quantities, the drag effect appears as the second-order solution that can equivalently be expressed as the product of two first order solution, u' and v' [see, e.g., Eq. (A2) of Hoepffner and Fukagata [10]]. Therefore, when the flow response is well described by the linear solution, we can predict the drag by substituting the first order solution in to Eq. (1). Namely, we can predict the drag increment, ΔD, (which is essentially the nonlinear effect) from the linear solution. The results obtained by these calculations are linear solutions so that the disturbance components are scaled by the wave amplitude, a.

While the Orr-Sommerfeld (OS) operator formulation used by Min *et al.* [8] is usually preferred to study this kind of problem [20,21], here we use the alternative formulation based on the primitive variables. Although these two formulations are mathematically equivalent, the present formulation has an advantage that it can be easily extended to include control inputs other than blowing and suction, e.g., body forces due to local heating and cooling [22,23], magnetohydrodynamics (MHD) [24], or plasma actuators (e.g., [25]), which may be more realistic control input than blowing or suction. All we have to do is to add the terms of these effects, we do not need to play with algebra beforehand. The result obtained with the same number of nodes should be more accurate than that with the OS formulation because the OS has a fourth order derivative whereas the derivative in the presented formulation is at highest second order. Increase in computational cost is subtle with the current computer power.

Figure 2 shows the dependency of the computed amount of drag reduction on the number of Chebyshev nodes. The difference between the values obtained with 128 nodes (used throughout the present study) and 512 nodes was less than 10^{-12} for both cases presented in Fig. 2.

III. RESULTS AND DISCUSSIONS

A. Varicose mode

Figure 3 shows the drag increment, ΔD, as a function of the wave speed of the traveling wave, c, computed at Re =2000 under different wave numbers, $k=0.5$, 1.0, 1.5, and 2.0. It confirms that the present method perfectly reproduces
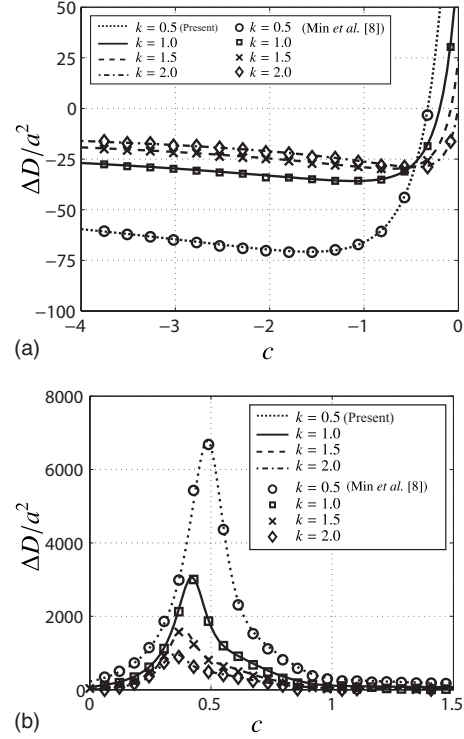

FIG. 3. Normalized drag increment, $\Delta D/a^2$, as a function of the wave speed, c, under different k (Re=2000, varicose mode): (a) upstream traveling waves, $c<0$; (b) downstream traveling waves, $c>0$.

the results of Min *et al.* [8]. For the upstream traveling wave as shown in Fig. 3(a), the drag decreases ($\Delta D<0$) by the faster traveling wave (i.e., the case of larger $|c|$). The amount of drag reduction is larger for smaller wave numbers. For the downstream traveling wave as shown in Fig. 3(b), ΔD is found to be positive. The drag is nearly unchanged in the range of $c>1$, whereas ΔD becomes extremely large in the range of $0<c<1$.

Figure 4 shows ΔD as a function of c for $k=0.5$ under different Reynolds numbers, Re=20, 200, 2000, and 10 000. At all Reynolds numbers, the drag is decreased by the faster upstream traveling wave. As increasing the Reynolds number, the effect of control becomes larger.

Two explanations can be made for the extremely large value of ΔD observed around $c=0.4$. One is the existence of a critical layer [10], which moves at the same speed of the wave speed of traveling wave as illustrated in Fig. 5. This layer is a singular point in the inviscid limit and the singularlike behavior still remains also in the viscous flow; thus, the velocity fluctuations, u' and v', are strongly amplified. Another is the quasiresonance between the forcing at the wall and the least stable mode of the governing equations. As has been shown by Lee *et al.* [15], the growth rate of the least stable mode takes the maximum around $c=0.4$.

Figure 6(a) shows the RSS distributions for $c=-1.5$ and Re=2000 under different wave numbers, $k=0.5$, 1.0, 1.5, and 2.0. It is clearly observed that the negative and positive RSSs are produced in the region near the lower and upper walls, respectively. According to Eq. (1), the skin-friction drag is the y-weighted integration of the RSS: the drag reduction,
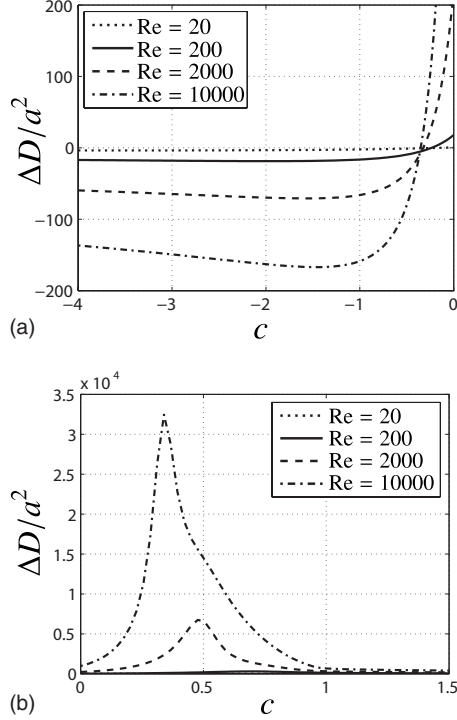
(a)

(b)

FIG. 4. Normalized drag increment, $\Delta D/a^2$, as a function of c at different Re ($k=0.5$, varicose mode): (a) upstream traveling waves $c<0$; (b) downstream traveling waves, $c>0$.
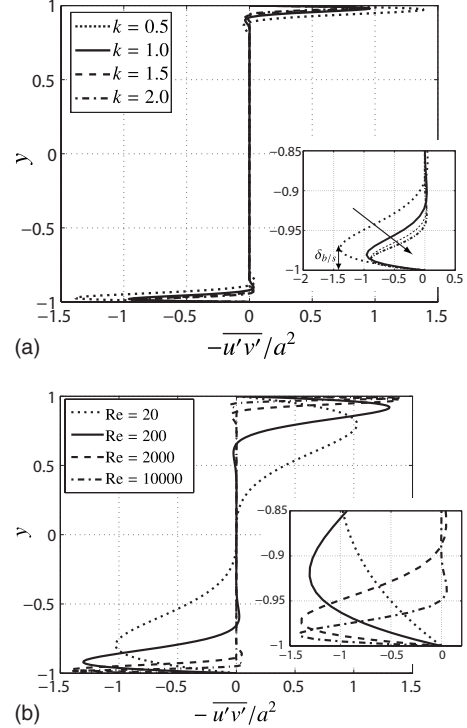

(a)

(b)

FIG. 6. Profile of the RSS induced by the varicose mode and the upstream ($c=-1.5$) traveling wave: (a) for different k, (Re=2000); (b) for different Re($k=0.5$).

$\Delta D<0$, observed above is due to the negative RSS induced in the region near the walls. Moreover, the zoom up of the near wall region in Fig. 6(a) shows that the peak of the RSS decreases as increasing the wave number. In this figure, we define an influence layer thickness of the traveling-wave-like blowing or suction, $\delta_{b/s}$, which is the height from the lower wall to the point of maximum $\left|-\overline{u'v'}\right|$. This influence layer thickness, $\delta_{b/s}$, is also found to decrease as increasing the wave number.

Figure 6(b) shows the RSS distributions for $c=-1.5$ and $k=0.5$ under different Reynolds numbers, Re=20, 200, 2000,

FIG. 5. (Color online) Schematic of a critical layer.

and 10 000. As increasing the Reynolds number, increase in maximum RSS and decrease in $\delta_{b/s}$ are observed.

These results imply that there is a relationship among the influence layer thickness, the wave number, and the Reynolds numbers. From the similarity of the problems, it may be natural to assume an analogy between the present flow and the Stokes' second problem. The Stokes' second problem is the steady oscillation of the wall under stationary fluid. The Stokes' layer thickness, δ_s, scales as

$$\delta_s\sqrt{\omega\,\mathrm{Re}} \simeq \mathrm{const}, \tag{10}$$

where ω is the angular frequency of the wall oscillation. We apply Eq. (10) to the case of traveling-wave-like blowing/suction, i.e., by substituting $\omega=|c|k$,

$$\delta_{b/s}\sqrt{|c|k\,\mathrm{Re}} \simeq \mathrm{const}, \tag{11}$$

where the left-hand side of Eq. (11) is referred hereafter as the dimensionless influence layer thickness.

This scaling is similar to that used for the analysis of skin-friction drag reduction induced by spanwise wall oscillations (e.g., [2]), although the detailed mechanism is somewhat different: in the spanwise oscillation the existing RSS is suppressed in the Stokes layer through the disruption of near-wall turbulence-production cycle [26,27]; while in the present case the RSS is actively produced in this layer.

Figure 7(a) shows the dimensionless influence layer thickness as functions of c for different wave numbers, k. The dimensionless influence layer thickness is found to be unchanged in the range of $c<-0.4$ and $c>1.0$, whereas it deviates from the constant value in the range where the critical
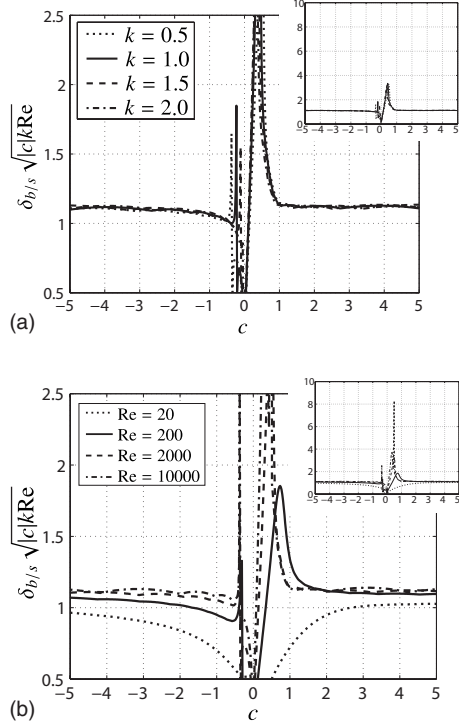
FIG. 7. The dimensionless influence layer thickness, $\delta_{b/s}\sqrt{|c|k}$ Re, as a function of c (varicose mode): (a) for different k (Re=2000); (b) for different Re(k=0.5).

layer effect is significant. The sub-figure shows dimensionless influence layer thickness in wider range of the vertical axis.

Figure 7(b) shows the dimensionless influence layer thickness at different Reynolds numbers. For the cases of Re=200, 2000, and 10 000, the dimensionless influence layer thickness is kept constant except for $|c| < 1$. The value for Re=20 are slightly lower than that for the other cases.

A schematic of the behavior of dimensionless influence layer thickness is shown in Fig. 8. The main reason for more peculiar behavior around $c=0$, where Stokes' analogy is not valid, may be threefold: (1) where $|c|$ approaches zero, $\delta_{b/s}$ does not infinitely increase due to the bounded domain; (2)
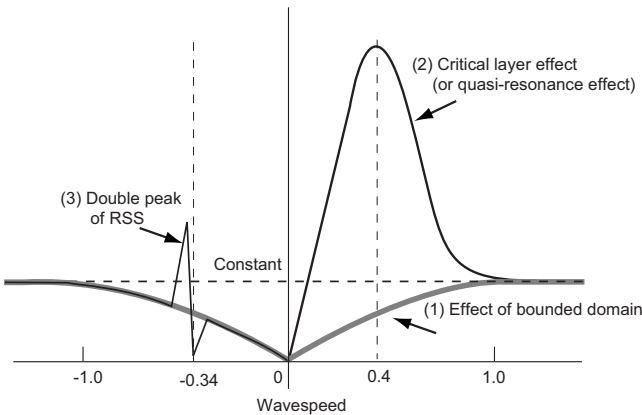
FIG. 8. Schematic of the dimensionless influence layer thickness: thick gray line, effect of bounded domain only; thin black line, actual behavior.
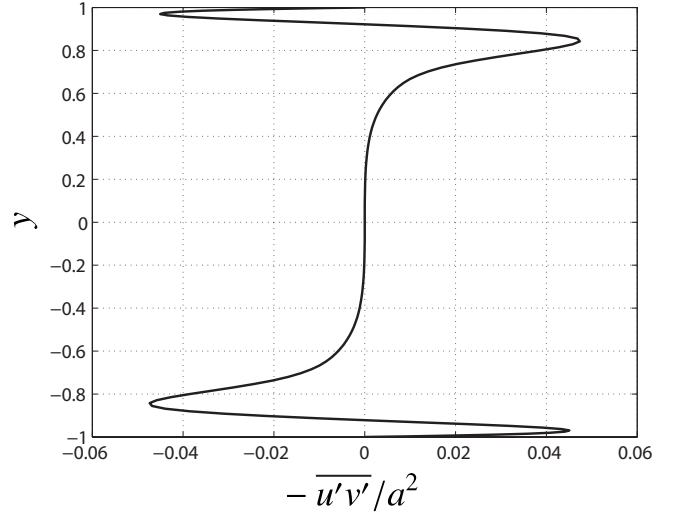
FIG. 9. Profile of the RSS when $\Delta D \approx 0$ induced by the varicose mode traveling wave. ($c=-0.34$, $k=0.5$, and Re=2000).

in the range of $0 < c < 1$ the effect of critical layer (or quasiresonance) appears; (3) around $c \approx -0.34$ the meaning of the defined influence layer thickness becomes ambiguous, where the RSS profile has double peaks (positive and negative) as exemplified in Fig. 9.

In the followings, a phase analysis is made to discuss the mechanism of the drag reduction in the range of c where the above analogy holds. The RSS can be expressed as the product of the absolute value of the Fourier coefficients and the phase difference, i.e.,

$$-\overline{u'v'} = -\frac{1}{2}|\hat{u}||\hat{v}|\sin(\phi), \qquad (12)$$

where ϕ is the phase difference between u' and v',

$$\phi = \arg\hat{u} - \arg\hat{v} + \frac{\pi}{2}. \qquad (13)$$

According to Eq. (12), nonzero RSS is created when u' and v' depart from the quadrature ($\phi=0$ or $\phi=\pm\pi$).

The sign of ΔD is determined by ϕ. Namely, the drag decreases when
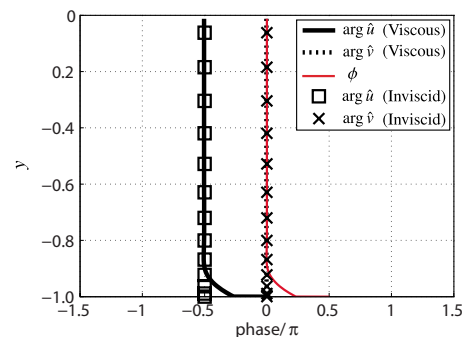

FIG. 10. (Color online) Profiles of phases of the Fourier coefficients for viscous and inviscid disturbances in drag reducing case by the upstream traveling wave (k=0.5, c=−1.5, Re=2000, and varicose mode).
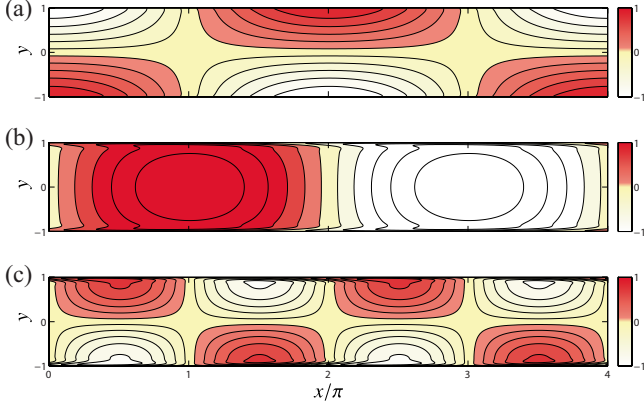
FIG. 11. (Color online) Disturbance fields: (a) v'/a, (b) u'/a, (c) $-u'v'/a^2$. The same condition as Fig. 10.

$$0 < \phi < \pi \quad (-1 < y < 0),$$

$$-\pi < \phi < 0 \quad (0 < y < 1), \qquad (14)$$

and the drag increases when

$$-\pi < \phi < 0 \quad (-1 < y < 0),$$

$$0 < \phi < \pi \quad (0 < y < 1). \qquad (15)$$

Again, this near-wall phase shift produces the RSS according to Eqs. (12)–(15).

Figure 10 shows the phase relationship between $\hat{u}$ and $\hat{v}$ in the lower half of the channel at the case of the maximum drag reduction. Hereafter, the ordinary phase relationship is defined as "viscous" phase relationship. The phase difference, ϕ, is found to be in the regions near the walls, and contributes the drag reduction according to Eq. (14). This nonquadrature is generated by the positive phase shift of $\hat{u}$, i.e., arg $\hat{v} = 0$ but arg $\hat{u} \neq -\pi/2$ in the region near the wall, as was pointed out by Min *et al.* [8].

Figure 10 also shows the phases computed from the inviscid linear equations [21], i.e., Eqs. (8) and (9) without the viscosity term, defined as "inviscid" phases. The inviscid
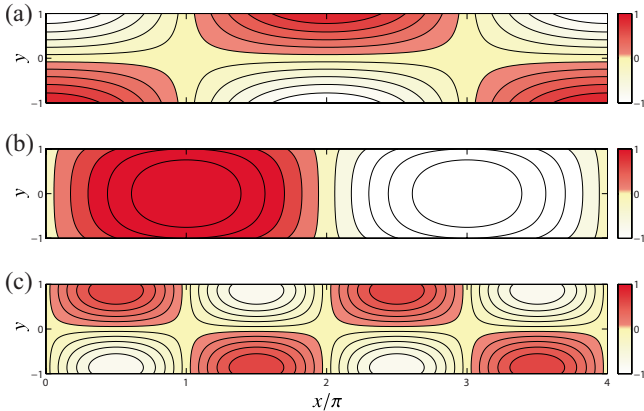
FIG. 12. (Color online) Disturbance fields computed from the inviscid equation: (a) v'/a, (b) u'/a, (c) $-u'v'/a^2$. The same condition as Fig. 10.
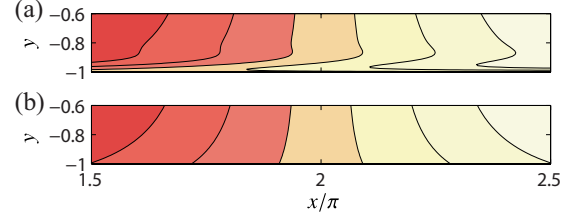
FIG. 13. (Color online) Zoom-up view of u' in the region near the wall: (a) viscous case [Fig. 11(b)] and (b) inviscid case [Fig. 12(b)].

phase relationship is found to be in quadrature. The viscous and inviscid phase relationships are similar except for the near-wall regions (hereafter which is defined as the "base phase relationship"). In the region near the wall, arg $\hat{u}$ (viscous) is found to lead arg $\hat{u}$ (inviscid), defined as the "near-wall phase shift." This viscous and inviscid comparison clearly shows that the near-wall phase shift is caused by the viscosity effect in the region near the wall. This region is the influence layer which is affected by the blowing or suction.

Figure 11 shows the disturbance fields of wall-normal velocity, v', streamwise velocity, u', and their product, $-u'v'$, respectively, at $k=0.5$, $c=-1.5$, and Re=2000. As shown in Fig. 11(a), the wall-normal velocity, v', induced by the traveling-wave-like blowing or suction is antisymmetric due to the varicose control input. Figure 11(b) shows symmetric u' generated as a response of the system. Due to the subtle phase shift of u' near the wall, u' and v' become nonquadrature and nonzero values of $-u'v'$ are created in the region near the wall as shown in Fig. 11(c). This $-u'v'$ is antisymmetric: negative and positive values appear more frequently near the lower and upper walls, respectively.

For comparison, the inviscid disturbance fields (computed by the inversed Fourier transformation of the solution of the inviscid linear equations) are depicted in Fig. 12. Again, the inviscid disturbance fields are found to be identical to the viscous disturbance fields except the region near the wall. Figure 13 shows the zoom-up view of u' in the region near the wall. The near-wall phase shift of viscous u' is clearly observed in the region near the wall. These results indicate that the base phase relationship is determined by the inviscid solution, whereas the near-wall phase shift, positive or negative, of streamwise velocity disturbance is induced by the
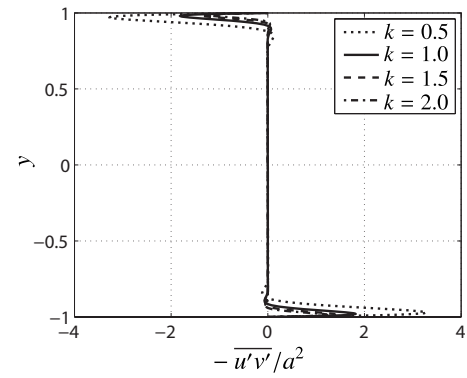

FIG. 14. Profile of the RSS induced by downstream ($c=1.5$) traveling wave for different k (Re=2000 and varicose mode).
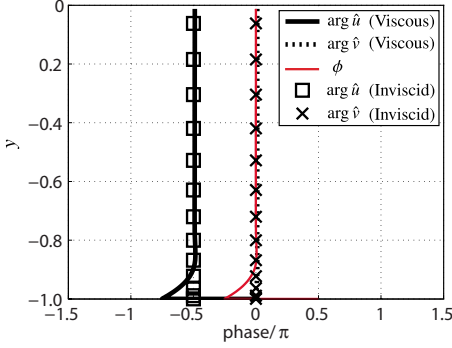
FIG. 15. (Color online) Profiles of phases of the Fourier coefficients for viscous and inviscid disturbances in drag increasing case by the downstream traveling wave ($k=0.5$, $c=1.5$, Re=2000, and varicose mode).

viscosity in the region near the wall and generates the non-quadrature between u' and v'.

The effect of the downstream traveling wave is also investigated. Figure 14 shows the RSS profile under $c=1.5$ and Re=2000 for different k. The RSS profile is found to be positive and negative in the region near the lower and upper walls, respectively, which produces the drag increase, $\Delta D > 0$, according to Eq. (1).

Figure 15 shows the viscous and inviscid phase relationships of the drag increase case ($k=0.5$, $c=1.5$, and Re =2000). It is clear that the drag increase can be explained by exactly the same argument (but with the opposite sign) as that made for drag reduction.
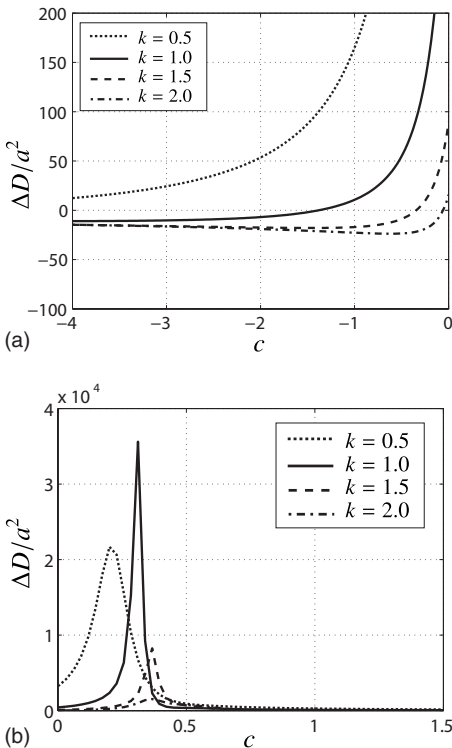
FIG. 16. Normalized drag increment, $\Delta D/a^2$ as a function of c under different k (Re=2000, sinuous mode): (a) upstream traveling waves ($c<0$) and (b) downstream traveling waves ($c>0$).
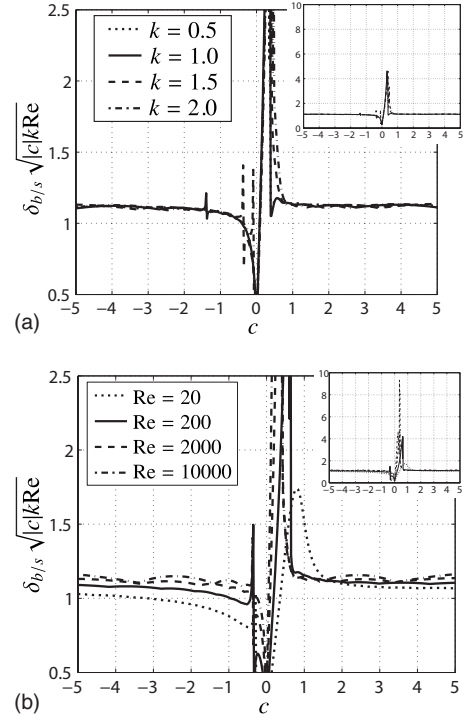
FIG. 17. The dimensionless influence layer thickness, $\delta_{b/s}\sqrt{|c|k}$ Re, as a function of wavespeed, c (sinuous mode): (a) for different k (Re=2000); (b) for different Re($k=1.5$).

B. Sinuous mode

Figure 16 shows the drag increment, ΔD, as a function of c, for the sinuous mode traveling wave. We obtain drag reduction ($\Delta D<0$) by the upstream traveling wave for $k=1.0$, 1.5, and 2.0. However, ΔD is found to be positive in the case of $k=0.5$. Similarly to the varicose mode, ΔD is found to be positive by the downstream traveling wave. A large drag increase is observed in the range of $0<c<0.5$ due to the critical layer and the flow instability. For the faster traveling wave, $c>0.5$, ΔD is found to approach zero.

Figure 17 shows that the dimensionless influence layer thickness, $\delta_{b/s}\sqrt{|c|k}$ Re, is kept constant in the range of $|c|>1$ regardless of k. The case of the Re=20 gives slightly lower values than the other cases of Re$\geq$200. This trend is common to the varicose mode.
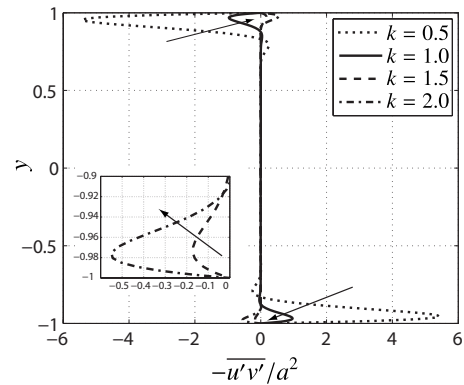

FIG. 18. Profile of the RSS induced by the sinuous mode traveling wave for different k ($c=-0.5$ and Re=2000).
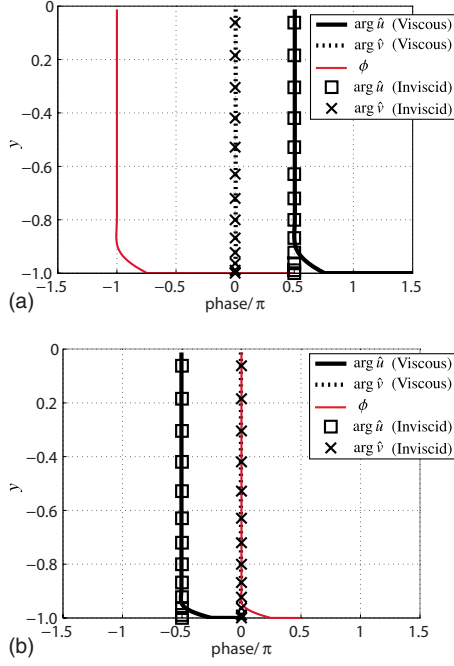
FIG. 19. (Color online) Profile of the phase of the Fourier coefficients for viscous and inviscid disturbance induced by the sinuous mode traveling wave ($c=-1.5$ and Re=2000): (a) $k=0.5$; (b) $k=2.0$.

Figure 18 shows the RSS profile under different k at $c=-0.5$ and Re=2000. The RSS for $k=0.5$ and $k=1.0$ is found to be negative and positive in the region near the upper and lower walls, respectively, which corresponds to the drag increase. As increasing the wave number, the peak of the RSS is found to decrease and becomes negative which leads to the drag reduction.

The phase relationships in the lower half of channel for $k=0.5$ and $k=2.0$ are shown in Figs. 19(a) and 19(b), respectively. In both cases, nonquadrature appears in the region near the wall due to the positive phase shift of arg $\hat{u}$ (viscous). Whereas the nonquadrature in $k=2.0$ results in drag reduction similar to that in the varicose mode that for $k=0.5$ leads to the drag increase. This is due to the difference of the base phase relationship, i.e., $\hat{u}=-\pi/2$ for $k=2.0$ (similarly to the varicose mode), arg $\hat{u}=\pi/2$ for $k=0.5$ (opposite to the varicose mode). This difference can better be understood by the streamlines, as shown in Fig. 20. Whereas the blowing from both walls (i.e., varicose mode) accelerate the
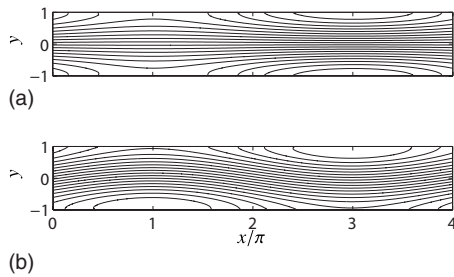

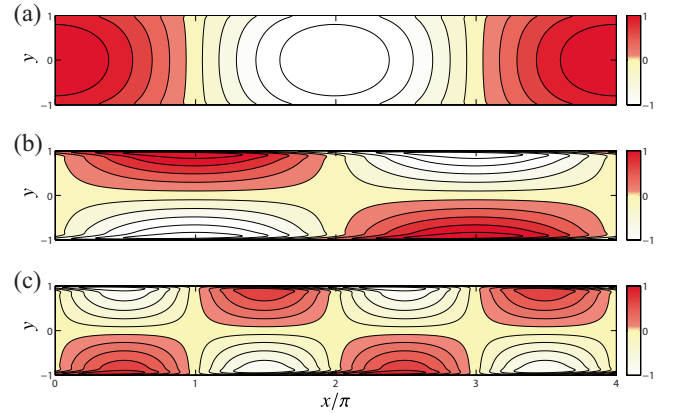FIG. 20. Streamline by the wave of (a) varicose mode and (b) sinuous mode ($k=0.5$, $c=-1.5$, and Re=2000).

FIG. 21. (Color online) Disturbance fields at $k=0.5$ (sinuous mode, $c=-1.5$, and Re=2000): (a) v'/a; (b) u'/a; (c) $-u'v'/a^2$.

bulk flow similarly to a contraction, blowing and suction from each wall (i.e., the sinuous mode) laterally displaces the fluid to result in deceleration (acceleration) of the bulk flow on the blowing (suction) side.

The distributions of velocity disturbances and their products for $k=0.5$ are shown in Fig. 21. Large v' appears in the center region of the channel as shown in Fig. 21(a) because the wall-normal velocity blown from the lower (upper) directly penetrates into the upper (suction) region due to the small wave number, $k=0.5$ (i.e., long wavelength). The vertical fluid motion induces u' as shown in Fig. 21(b). Unlike the cases of varicose mode (Figs. 11 and 12) and the cases of sinuous mode at higher wave numbers (Fig. 22), the base phase of u' delays and leads $\pi/2$ from that of v' in the upper and lower half region, respectively. Although, the near-wall phase shift of u' in the region near the wall is induced in exactly the same manner as that for the varicose mode, the difference in the base phase relationship results in the dominance of positive $-u'v'$ [Fig. 21(c)] and the drag increase.

C. Parametric study

The dimensionless influence layer thickness and the phase relationship are computed for wider range of parameters. We compute about 500 000 cases for the varicose and the sinuous modes, in the range of $0.01<k<5$ and $-5<c<5$. The intervals of k and c are set to be 0.01.

Figures 23(a) and 23(b) show the maps of the dimensionless influence layer thickness by the varicose and sinuous mode traveling waves, respectively. The dimensionless influence layer thickness is found to be constant, except for the region near $c\simeq0$, which confirms that the analogy between present control and Stokes' second problem holds in wider ranges of parameters.

In the previous subsections, the phase analysis explains the mechanism: the nonquadrature between velocity disturbances creates the RSS which generates ΔD. The nonquadrature appears as the phase difference, ϕ. In order to make a unified explanation for all cases studied, we propose the following decomposition of ϕ:

$$\phi = \Phi + \alpha. \tag{16}$$

Here, Φ is the base phase difference defined as the departure from quadrature determined by the inviscid disturbance, i.e.,

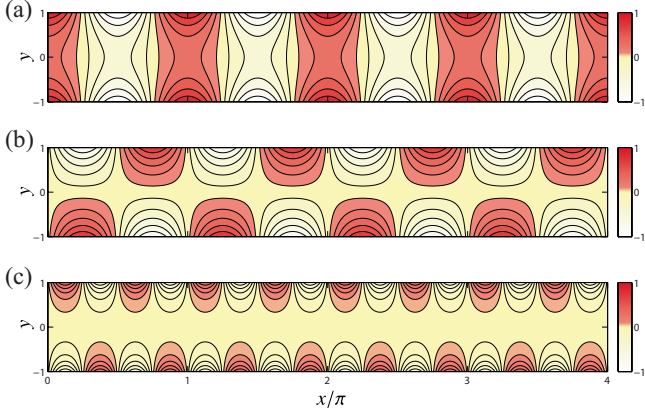FIG. 22. (Color online) Disturbance fields at $k=2.0$ (sinuous mode, $c=-1.5$, and Re=2000): (a) v'/a; (b) u'/a; (c) $-u'v'/a^2$.

$$\Phi = \arg \hat{u}(\text{inviscid}) - \arg \hat{v}(\text{inviscid}) + \frac{\pi}{2}, \qquad (17)$$

and α is the near-wall phase shift, which is defined as the difference between the arg $\hat{u}$ (viscous) and the arg $\hat{u}$ (inviscid), i.e.,

$$\alpha = \arg \hat{u}(\text{viscous}) - \arg \hat{u}(\text{inviscid}). \qquad (18)$$

This decomposition enables us to easily overview the effect of the base and the near-wall phase relationship on the drag for different parameter sets of c and k. For convenience, the base phase difference, Φ, and the near-wall phase shift, α, are computed where $|-\overline{u'v'}|$ takes maximum value in the lower half of the channel.

Figure 24 shows the distributions of Φ, α, and ΔD by the varicose mode traveling wave at Re=2000. The phase and ΔD are normalized by π and a^2, respectively. Figure 24(a) shows that Φ is zero in the most regions in accordance with Fig. 10.

Figure 24(b) shows the distribution of the near-wall phase shift, α/π: the upstream traveling wave ($c<0$) creates the positive phase shift of streamwise velocity as visualized in Fig. 11 and the downstream traveling wave ($c>0$) induces negative phase shift. The sign of α/π does not depend on k. The phase difference, ϕ, which consists of Φ and α, results in

$$0 < \phi < \pi \quad (c < 0), \qquad (19)$$

$$-\pi < \phi < 0 \quad (c > 0), \qquad (20)$$

in the lower half region of the channel. According to Eqs. (14) and (15), the drag reduction and increase are obtained by the upstream and the downstream traveling waves, respectively, as confirmed by Fig. 24(c).

The phase relationship and ΔD in the case of sinuous mode traveling wave are shown in Fig. 25. Although the phase relationships, Φ and α, are basically similar to those of the varicose mode, a region of $\Phi/\pi=1$ is found for small k and $c<0$. This is due to the penetration of wall-normal velocity as observed in Fig. 21. Accordingly, the phase difference, ϕ, becomes
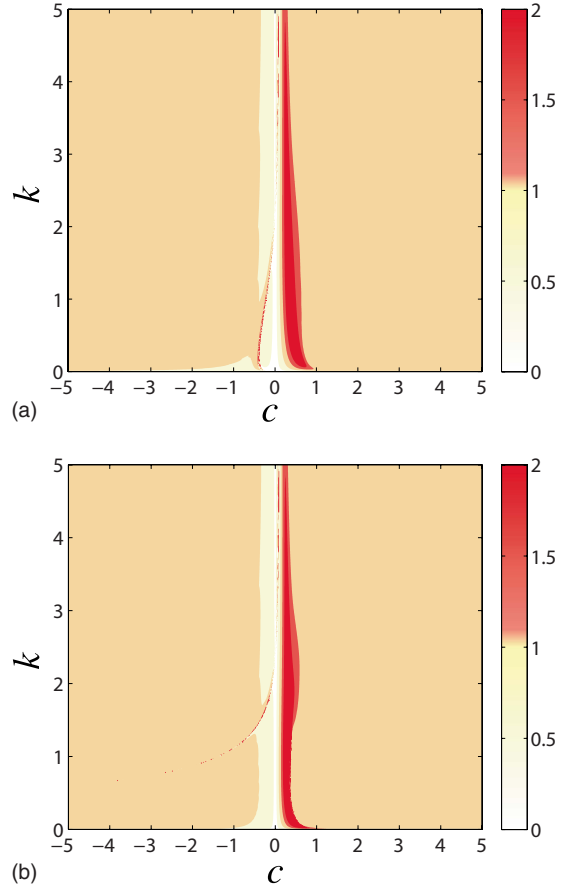

FIG. 23. (Color online) Map of the dimensionless influence layer thickness (Re=2000): (a) varicose mode; (b) sinuous mode.

$$0 < \phi < \pi \quad (c < 0, \text{small } k), \qquad (21)$$

$$-\pi < \phi < 0 \quad (\text{otherwise}), \qquad (22)$$

in the lower half region of the channel. These ϕ lead the drag reduction and increase as shown in Fig. 25(c), respectively.

IV. CONCLUSIONS

The skin-friction drag reduction mechanism by the traveling-wave-like blowing or suction control of Min *et al.* [8] is investigated in the two-dimensional laminar Poiseuille flow. The velocity disturbances are computed by the linear analysis with the Chebyshev collocation point method. The drag increment by the control input is predicted by using the identity equation between the skin-friction drag increment and the Reynolds shear stress [6,7].

It is confirmed that the analogy between the present control and the Stokes' second problem holds. The dimensionless influence layer thickness is found to be constant, for different parameters, k, c, and Re, and the wave modes (the varicose and the sinuous modes). This scaling is similar to that used for the analysis of drag reduction by spanwise wall oscillation.

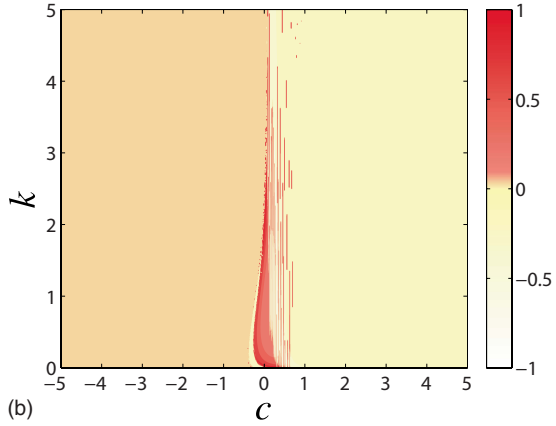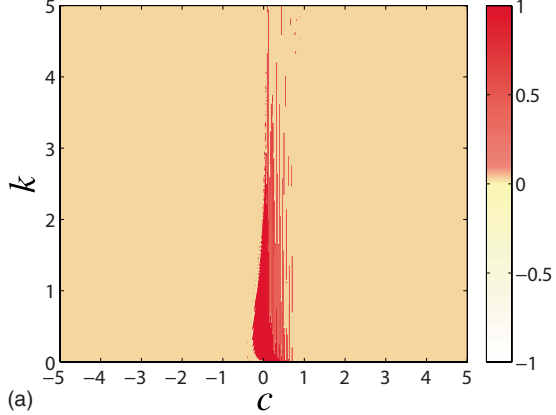The phase analysis shows the mechanism of the drag reduction and increase. The Reynolds shear stress, which con-

FIG. 24. (Color online) (a) The base phase difference, Φ/π; (b) the near-wall phase shift, α/π; (c) the drag increment, $\Delta D/a^2$. Varicose mode (Re=2000).

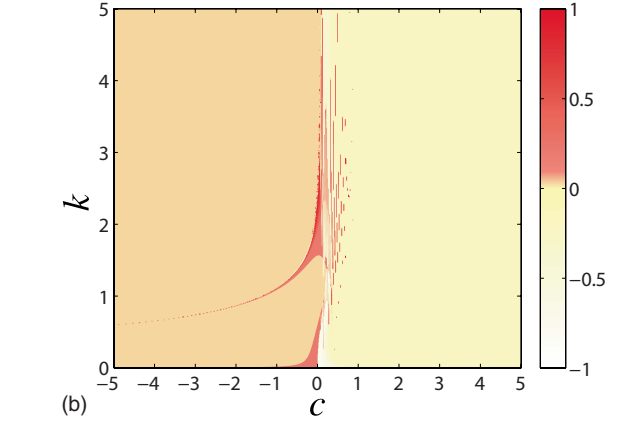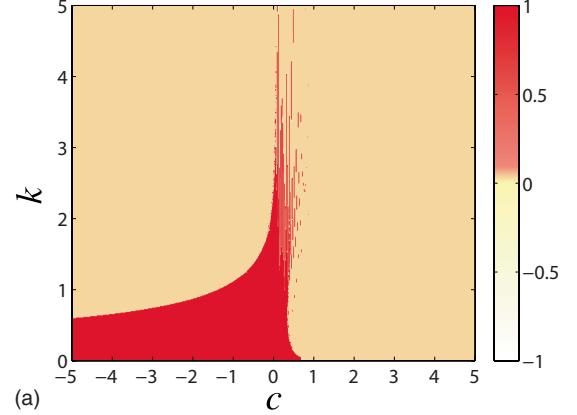FIG. 25. (Color online) (a) The base phase difference, Φ/π; (b) the near-wall phase shift, α/π; (c) the drag increment, $\Delta D/a^2$. Sinuous mode (Re=2000).

tributes to the drag increment from the laminar level, is induced by the nonquadrature between velocity disturbances. This nonquadrature is decomposed to the base phase relationship and near-wall phase shift. The base phase relationship agrees with that by the solution of the inviscid disturbance equations. For the case of the varicose mode, the base phase relationship is found to be independent of wave number, i.e., v' leads $\pi/2$ from u' in the lower half region of the channel. For the sinuous mode, the phase reversal of u' is observed at the small wave numbers (i.e., long wavelength). In the region near the walls, the viscosity induces the near-wall phase shift. The upstream and downstream traveling waves induce the negative and positive phase shift of streamwise velocity, respectively, for the both wave modes.

APPENDIX: NUMERICAL DISCRETIZATION

The detailed procedure to solve the linearized Navier-Stokes equation [Eqs. (7)–(9)] under the boundary condition [Eq. (5)] is explained here.

Due to the periodic boundary condition assumed in the streamwise direction, the Fourier transformation can be applied for the state variable vector, $\mathbf{q}' = (\mathbf{u}', \mathbf{v}', \mathbf{p}')^T$, as

$$\mathbf{q}' = \mathscr{R}[\hat{\mathbf{q}}(y)\exp(ikx)], \tag{23}$$

where $\mathscr{R}$ is a real part. In the wall-normal direction, the Fourier coefficients are discretized by using the Chebyshev collocation point method: the Chebyshev differentiation matrix of a MATLAB function, chebdif.m provided by Wiedman and Reddy [28], is applied for the y-derivative operators to obtain the discretized state vector,

$$\hat{\mathbf{q}} = (\hat{\mathbf{u}}, \hat{\mathbf{v}}, \hat{\mathbf{p}})^T. \tag{24}$$

As a result of these transformations, Eqs. (7)–(9) are expressed as a system matrix equation,

$$\mathbf{A}\hat{\mathbf{q}} = \mathbf{b}, \tag{25}$$

of which concrete form is graphically shown in Fig. 26, where the operator $\mathbf{L}_1$ reads

FIG. 26. (Color online) Schematic of the system matrix equation with the boundary conditions. The blocks correspond to the discretized version of Eqs. (7)–(9).

$$\mathbf{L}_1 = ik(\mathbf{U} - c\mathbf{I}) - \frac{1}{\mathrm{Re}}(\mathbf{D}_2 - k^2\mathbf{I}), \tag{26}$$

and $\mathbf{D}_1$ and $\mathbf{D}_2$ are the Chebyshev first- and second-order differentiation matrices, respectively, and $\mathbf{I}$ is the unit matrix. The boundary conditions read

$$\hat{v}_{w\pm} = \begin{cases} \mp a & \text{varicose mode} \\ \pm a & \text{sinuous mode}. \end{cases} \tag{27}$$

The boundary conditions are included in the system matrix, $\mathbf{A}$, and the right-hand side, $\mathbf{b}$, as shown in Fig. 26. Thus, the solution of the matrix equation can be simply obtained by

$$\hat{\mathbf{q}} = \mathbf{A}^{-1}\mathbf{b}, \tag{28}$$

and spatial distributions of u', v', and p' are computed by the inversed Fourier transform to the solution. Finally, ΔD is computed by using Eq. (1).

[1] M. Gad-el-Hak, AIAA J. **32**, 1753 (1994).
[2] G. E. Karniadakis and K.-S. Choi, Annu. Rev. Fluid Mech. **35**, 45 (2003).
[3] H. Choi *et al.*, J. Fluid Mech. **255**, 503 (1993).
[4] T. Endo *et al.*, Int. J. Heat Fluid Flow **21**, 568 (2000).
[5] S. Kang and H. Choi, Phys. Fluids **12**, 3301 (2000).
[6] K. Fukagata *et al.*, Phys. Fluids **14**, L73 (2002).
[7] T. R. Bewley and O. M. Aamo, J. Fluid Mech. **499**, 183 (2004).
[8] T. Min *et al.*, J. Fluid Mech. **558**, 309 (2006).
[9] I. Marusic *et al.*, J. Fluid Mech. **570**, 467 (2007).
[10] J. Hoepffner and K. Fukagata, J. Fluid Mech. **635**, 171 (2009).
[11] P. Luchini, *Progress in Industrial Mathematics at ECMI 2006*, Mathematics in Industry, Vol. 12 (Springer, New York, 2008), p. 169.
[12] N. Kasagi *et al.*, *Advances in Turbulence XII*, Springer Proceedings in Physics, Vol. 132 (Springer, Berlin, 2009), p. 189.
[13] B. Lieu *et al.* (unpublished).
[14] R. Moarref and M. R. Jovanović (unpublished).
[15] C. Lee *et al.*, Phys. Fluids **20**, 101513 (2008).
[16] N. Kasagi *et al.*, Annu. Rev. Fluid Mech. **41**, 231 (2009).

[17] T. R. Bewley, J. Fluid Mech. **632**, 443 (2009).
[18] K. Fukagata *et al.*, Physica D **238**, 1082 (2009).
[19] M. R. Jovanović *et al.*, Center for Turbulence Research Proceeding of the Summer Program 2006, 2006 (unpublished), p. 481.
[20] P. G. Drazin and W. H. Reid, *Hydrodynamic Stability* (Cambridge University, New York, 1981).
[21] P. J. Schmid and D. S. Hennninngson, *Stability and Transition in Shear Flow* (Springer, New York, 2001).
[22] H. S. Yoon *et al.*, Phys. Fluids **18**, 025104 (2006).
[23] H. Mamori *et al.*, Proceeding of the Sixth International Symposium on Turbulence and Shear Flow Phenomena, Seoul, Korea, 2009 (unpublished), p. 581.
[24] Y. Du and G. E. Karniadakis, Science **288**, 1230 (2000).
[25] W. Shyy *et al.*, J. Appl. Phys. **92**, 6434 (2002).
[26] J.-I. Choi *et al.*, AIAA J. **40**, 842 (2002).
[27] P. Ricco and M. Quadrio, Int. J. Heat Fluid Flow **29**, 891 (2008).
[28] J. A. Weideman and S. C. Reddy, ACM Trans. Math. Softw. **26**, 465 (2000).